



## RESEARCH LETTER

10.1002/2014GL060801

## Key Points:

- First quantitative retrieval of the terrestrial K layer from space
- The unusual semiannual behavior of K is near global in extent

## Correspondence to:

J. M. C. Plane,  
j.m.c.plane@leeds.ac.uk

## Citation:

Dawkins, E. C. M., J. M. C. Plane, M. P. Chipperfield, W. Feng, J. Gumbel, J. Hedin, J. Höffner, and J. S. Friedman (2014), First global observations of the mesospheric potassium layer, *Geophys. Res. Lett.*, *41*, 5653–5661, doi:10.1002/2014GL060801.

Received 6 JUN 2014

Accepted 19 JUL 2014

Accepted article online 23 JUL 2014

Published online 4 AUG 2014

## First global observations of the mesospheric potassium layer

E. C. M. Dawkins<sup>1,2</sup>, J. M. C. Plane<sup>1</sup>, M. P. Chipperfield<sup>2</sup>, W. Feng<sup>1,2</sup>, J. Gumbel<sup>3</sup>, J. Hedin<sup>3</sup>, J. Höffner<sup>4</sup>, and J. S. Friedman<sup>5,6</sup>

<sup>1</sup>School of Chemistry, University of Leeds, Leeds, UK, <sup>2</sup>School of Earth and Environment, University of Leeds, Leeds, UK,

<sup>3</sup>Department of Meteorology, Stockholm University, Stockholm, Sweden, <sup>4</sup>Leibniz-Institute for Atmospheric Physics, University of Rostock, Kühlungsborn, Germany, <sup>5</sup>SRI International Arecibo Observatory, Arecibo, Puerto Rico, <sup>6</sup>Puerto Rico Photonics Institute, Universidad Metropolitana, Barceloneta, Puerto Rico

**Abstract** Metal species, produced by meteoric ablation, act as useful tracers of upper atmosphere dynamics and chemistry. Of these meteoric metals, K is an enigma: at extratropical latitudes, limited available lidar data show that the K layer displays a semiannual seasonal variability, rather than the annual pattern seen in other metals such as Na and Fe. Here we present the first near-global K retrieval, where K atom number density profiles are derived from dayglow measurements made by the Optical Spectrograph and Infrared Imager System spectrometer on board the Odin satellite. This robust retrieval produces density profiles with typical layer peak errors of  $\pm 15\%$  and a 2 km vertical grid resolution. We demonstrate that these retrieved profiles compare well with available lidar data and show for the first time that the unusual semiannual behavior is near-global in extent. This new data set has wider applications for improving understanding of the K chemistry and of related upper atmosphere processes.

### 1. Introduction

Changes in the mesosphere may be an important signal of climate change, and there is increasing evidence that accurate simulations of changes to the Earth's climate require models with a well-resolved and accurate stratosphere and mesosphere [e.g., see Akmaev, 2011; Hurrell et al., 2013]. Coupling exists between all regions of the atmosphere in terms of mass, momentum, and energy exchange, and an understanding of the processes which occur in the middle atmosphere will give a greater understanding of our atmosphere as a whole [e.g., see Roble and Dickinson, 1989; Akmaev et al., 2006; Laštovička, 2006; Chandran et al., 2013].

A current gap in knowledge concerns the huge uncertainty in the amount of interplanetary dust entering the Earth's atmosphere from space, with estimates varying from 5 to 300 t d<sup>-1</sup> [Plane, 2012]. The main sources of cosmic dust in the solar system are from collisions between asteroids and from sublimating comets on their approach to the Sun. These dust particles enter the Earth's atmosphere at velocities between 11 and 71 km s<sup>-1</sup>, causing ablation which injects metal atoms and ions into the mesosphere/lower thermosphere region (MLT) (75–110 km). The resulting layers of metal atoms provide a unique way of observing this region and of testing chemistry-climate models [Plane, 2003].

### 2. Current Observations

Much progress has been made in the last two decades in understanding the mesospheric metal layers through a combination of (mostly) lidar observations, laboratory studies of relevant physicochemical parameters, and atmospheric modeling [see, e.g., Plane, 2003; Feng et al., 2013; Marsh et al., 2013].

A large amount of lidar data exist for Na and Fe, in part as a result of the importance of their use to determine upper atmospheric temperatures and wind profiles. In contrast, there are only two stations which measure K, Arecibo in Puerto Rico (18.3°N, 293.2°E) and Kühlungsborn in Germany (54.1°N, 11.8°E). A number of studies using data from these stations have been published [von Zahn and Höffner, 1996; Eska et al., 1998, 1999; Delgado et al., 2012], along with data from a ship-borne Atlantic transect [Eska et al., 1999], limited data from Haute-Provence (44°N) [Mégie et al., 1978], Tenerife (28°N) [Fricke-Begemann et al., 2002], and Spitsbergen (78°N) [Höffner et al., 2003; Lübken and Höffner, 2004; Höffner and Lübken, 2007; Raizada et al., 2007]. Satellite work so far has focused on atomic Na [Fussen et al., 2004, 2010; Fan et al., 2007; Gumbel et al.,

This is an open access article under the terms of the Creative Commons Attribution License, which permits use, distribution and reproduction in any medium, provided the original work is properly cited.

2007; Fussen et al., 2010; Hedin and Gumbel, 2011] and magnesium [Gardner et al., 1995; Scharringhausen et al., 2008a, 2008b; Langowski et al., 2014a, 2014b].

While the Na, Fe, and Mg atom (and singly ionized Mg<sup>+</sup>) number densities all show an annual seasonal dependence (wintertime maximum and summertime minimum), the limited K lidar observations show that the atomic K layer exhibits semiannual variability with maxima in both winter and summer, and equinoctial minima. Understanding this different and unusual seasonal behavior of K currently remains an unsolved problem.

With only two operational lidar stations, the global distribution of K can only be obtained using satellite-borne observations. This paper provides an overview of a new K retrieval method based on an existing Na scheme [Gumbel et al., 2007]. The capabilities of the K retrieval are discussed and demonstrated via comparison with available lidar data. Finally, the first near-global observations of the K layer are presented.

### 3. Description of the Potassium Retrieval Algorithm

Launched in February 2001, the Sun-synchronous and polar-orbiting Odin satellite is a dual-purpose aeronomy and astronomy mission designed and managed by a Swedish/Canadian/Finnish/French consortium. Onboard are two instruments; the Optical Spectrograph and Infrared Imager System (OSIRIS) and the Submillimeter Radiometer (SMR) [Murtagh et al., 2002; Llewellyn et al., 2004].

The OSIRIS instrument measures limb-scattered sunlight across the wavelength range 280–810 nm with a pixel resolution of 0.4 nm and a spectral resolution of 1 nm. The instrument field of view is approximately 1 km vertically and 40 km horizontally, when mapped onto the atmospheric limb at the tangent point. The satellite scans in the limb from 5 to 110 km with a typical height resolution of 1.5–2 km within the mesosphere. OSIRIS has two local sampling times of 0600 and 1800 LT and covers the latitude range of 82°N to 82°S. As it records a useable signal during daylight conditions only, there is limited coverage in the winter hemisphere at middle to high latitudes.

The retrieval scheme developed by Gumbel et al. [2007] is an optimal estimation method [after Rodgers, 2000] which uses a forward model to convert observed limb radiances from OSIRIS into vertically resolved metal number densities. The observed spectra are modeled by integrating the radiation scattered toward the instrument along the line of sight in a spherical atmosphere, with background temperature and density profiles taken from the Mass Spectrometer Incoherent Scatter atmospheric model [Hedin, 1991] and European Centre for Medium-Range Weather Forecasts reanalyses [Dee et al., 2011].

The basic concept for the retrieval is

$$y = F(x, b) + \varepsilon \tag{1}$$

where  $y$  = measured vertical radiance profile,  $F$  = forward model,  $x$  = retrieved vertical K density,  $b$  = important but nonretrieved relevant parameters (e.g., albedo and reference solar irradiance spectrum), and  $\varepsilon$  = measurement error.

This retrieval problem is close enough to linear to allow it to be inverted using Gauss-Newton iteration, thus becoming

$$x_{i+1} = x_a + G_i[y - F(x_i) + K_i(x_i - x_a)] \tag{2}$$

where  $K_i$  = weighting function matrix ( $K_i = \partial F(x_i) / \partial x$ ) and  $G_i$  = contribution function matrix ( $G_i = \partial x / \partial y = S_a \cdot K_i^T \cdot (K_i \cdot S_a \cdot K_i^T + S_e)^{-1}$ ) for iteration,  $i$ . The covariance of the measurements is  $S_e$ . The retrieval problem does not have a unique solution (it is formally ill posed) and an a priori number density profile, and its associated covariance is required to regularize the solution;  $x_a$  represents a priori knowledge based on a single annual mean midlatitude K lidar profile (from Kühlungsborn) and is shown in Figure 2d, along with the associated covariance ( $S_a$ ). The covariance was chosen to reflect the large amount of natural variability seen within both the Arecibo and Kühlungsborn lidar observations. The a priori profile serves as a starting point for the retrieval and provides regularization so that a unique solution may be found. The forward model is slightly nonlinear due to line absorption, and thus, an iterative approach must be employed. With successive iterations,  $x_i$  converges to final value  $x$ . A convergence limit (2 atoms  $\text{cm}^{-3}$ ) is set, and the retrieval stops iterating when either successive retrieved profiles differ less than this convergence limit or the maximum number of iterations

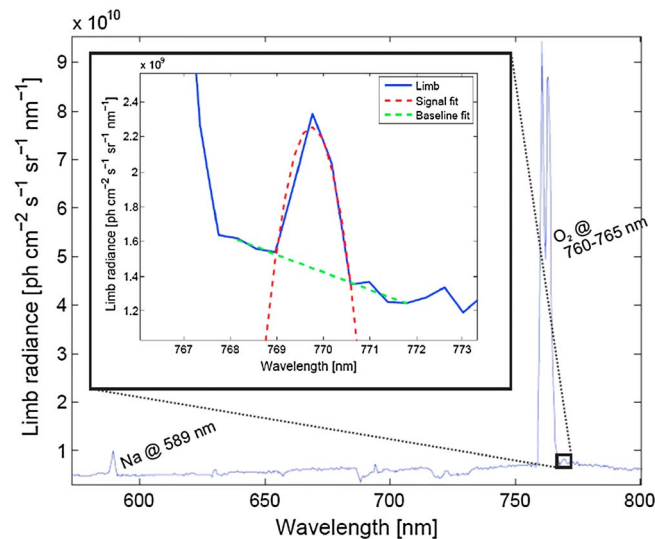


**Figure 1.** Extracting the K emission signal. An example 90 km limb radiance spectrum (575–810 nm) is shown with the Na resonance line at 589 nm, and the O<sub>2</sub> A-band line at 760–765 nm labeled. The inset is a close-up of the potassium resonance line at ~770 nm. This has been normalized with the corresponding 40 km limb spectrum (from the same scan) with the peak center wavelength pixel set to unity. This effectively removes the Fraunhofer lines and any structure present in both peak layer altitude spectra and those at lower stratospheric altitudes. A second-order polynomial (red) is fitted to the peak region (769.96–770.58 nm). A first-order polynomial (green) is fitted to the background regions either side. The area bounded between the signal curve and background baseline is then integrated to produce the total K emission (units:  $\text{ph cm}^{-2} \text{s}^{-1} \text{sr}^{-1}$ ).

altitude, multiple scattering from higher altitudes is assumed to be negligible. This albedo contribution is then combined with the direct solar irradiance at the OSIRIS line of sight. The spectroscopic properties of the K atom are considered (i.e., scattering cross section and transition probabilities) [Kramida *et al.*, 2013] along with wavelength-dependent features such as the incident solar irradiance and shape of the spectral background. Currently, only the most abundant naturally occurring isotope <sup>39</sup>K (at 93.2%) and first-order hyperfine splitting is considered. The Ring effect, which increases the photon flux in the Fraunhofer minima [Chance and Spurr, 1997] and can contribute to additional illumination of the K layer, is generally less than 5% with a limited effect on the retrieved densities (see Langowski *et al.* [2014a] for further details). Thus, the Ring effect has been neglected in the current retrieval algorithm.

Similar to Na at 589 nm, K has two D lines at 769.90 nm (D<sub>1</sub> line) and 766.49 nm (D<sub>2</sub> line). The K D<sub>2</sub> line is stronger than the D<sub>1</sub> line but is obscured by the much stronger O<sub>2</sub> A-band at 760–765 nm, so only the D<sub>1</sub> line is used in this study. The retrieval of K represents a much greater challenge than that of Na. While both Na and K have very similar, large absorption cross sections (the peak cross section for the K D<sub>1</sub> line is  $1.3 \times 10^{-11} \text{ cm}^2 \text{ atom}^{-1}$  at 200 K, calculated from the Einstein coefficient of  $3.82 \times 10^7 \text{ s}^{-1}$  [Lide, 2006]), the atmospheric abundance of K in the MLT is roughly a factor 50 smaller than that of Na. The K D<sub>1</sub> line is also in the near-IR where solar irradiance is smaller, and is within the vicinity of the shoulder of the A-band (Figure 1). For these reasons the resonance line has a much poorer signal-to-background ratio than that of Na at 589 nm. A final consideration is that it is likely that the quantum efficiency of the OSIRIS spectrometer CCD (charge-coupled device) detector has degraded more at these longer wavelengths [Llewellyn *et al.*, 2004].

The radiance detected in the satellite instrument's line of sight consists of discrete emission/absorption features superimposed over broader Rayleigh and Mie scattering features. In order to quantify the K density from a radiance scan, it is important to discriminate between metal fluorescence and background radiation. Figure 1 illustrates how vertical radiance profiles are derived from limb radiance spectra. Polynomial functions are fitted to the K signal (768.96–770.58 nm) and background (768.15–768.96 nm and 770.58–771.80 nm) regions of a

(maximum of 10 permitted) has been reached. This iteration limit is imposed to ensure computational running efficiency of the retrieval. The majority of profiles converge within less than five iterations, and a profile is rejected if there is no convergence within 10 iterations.

The forward model describes how the observed radiance in the instrument line of sight relates to the metal atom density. A detailed description of the forward model can be found in Gumbel *et al.* [2007]. It includes ray tracing, extinction of incoming solar irradiance by metal atoms, resonant scattering out of the instrument line of sight, and transmission through the metal layer along with self-absorption by the metal atoms. The explicit radiative transfer simulation is restricted to single scattering, while multiple scattering is taken into account as a planetary albedo contribution from the ground and lower atmosphere. The albedo contribution is the ratio of the observed background radiances (either side of the K peak) to the equivalent simulated Rayleigh scattering at 40 km. At this

normalized limb radiance spectrum. A 40 km limb spectrum was used for the normalization, with this reference tangent height chosen as it was assumed that the metal signal in it would be negligible and it was sufficiently high in the stratosphere to avoid highly variable Mie scattering effects on the albedo at lower altitudes. Normalizing with this reference spectrum removes common structures present in both the reference and higher-altitude spectra, as well as accounting for Fraunhofer structure. While the K D<sub>2</sub> line is affected by the A-band, the D<sub>1</sub> line is not affected significantly. The radiance signal at the normalization tangent altitude shows limited A-band absorption at the D<sub>1</sub> wavelength. The fitting of the baseline to the background regions either side of the K peak accounts for any broadband changes in the background during the deconvolution of the spectrum.

An example vertical radiance profile derived from the above approach is shown in Figure 2 along with the resulting retrieved density profile and associated errors. The total error comprises the retrieval noise, model parameter error, forward model error, and smoothing error as shown in equation (3):

$$\hat{x} - x = \hat{G}\varepsilon + \hat{G}K_b(b - \hat{b}) + \hat{G}\Delta f(x, b) + (\hat{A} - I)(x - x_a) \quad (3)$$

The measurement noise ( $\hat{G}\varepsilon$ ) (where  $\hat{G}$  is the final contribution function) consists of the random errors in the processing of the OSIRIS CCD array into radiances, along with the errors introduced during the fitting routine when deriving the vertical radiance profiles. The forward model parameter error ( $\hat{G}K_b(b - \hat{b})$ ) includes errors predominantly resulting from uncertainty in determining the albedo ratio and solar irradiance reference spectrum. These errors are generally less than 15% at all altitudes. The forward model error ( $\hat{G}\Delta f(x, b)$ ) arises from incomplete knowledge of the physics relating the observed radiance to the metal number density. This error term is difficult to characterize. However, it is likely to be systematic in nature and comparisons with lidar observations (see below) indicate that it is small. The smoothing error ( $(\hat{A} - I)(x - x_a)$ ) describes the uncertainty in the observed vertical structure as a result of the limited vertical resolution of the retrieval. The retrieved profiles are smoothed by the averaging kernel ( $\hat{A}$ ) which results in a smoothing error. The relative contributions of the different error sources to the example retrieved density profile are shown in Figure 2c. The relative error contribution is lowest within the peak metal concentration region (around 15%), with the major contribution being the forward model parameter error. Above and below the peak region, the error increases largely as a result of an increasing smoothing error contribution, reaching a maximum of 50% of the total retrieved profile at 80 km and 70% at 101 km.

The vertical resolution of the retrieved profile can be determined from the full width at half maximum of the elements of the averaging kernel matrix (see Figure 2e). Within the peak region (83–101 km), the vertical resolution is approximately 2 km. The vertical resolution decreases to 4 km above and below this sensitive region.

#### 4. Ground-Truthing the Retrieved Profiles

A comparison of the mean K density profiles retrieved from OSIRIS for July 2004 and 2005 are compared against Arecibo (18°N) and Kühlungsborn (54°N) observations in Figures 3a and 3b, respectively. These years were chosen due to large temporal overlaps between the OSIRIS data and lidar operational periods. Each OSIRIS profile represents a zonal mean ( $\pm 5^\circ$  about the latitude of the lidar station). Monthly profiles are used because both data sets are intermittent (the OSIRIS instrument does not operate continuously due to split commitments for Odin operating in aeronomy versus astronomy mode). The error of the mean ( $2\sigma$ ) is used as the error range for the satellite data; these measurements are largely spatiotemporally independent. However, due to the nature of lidar measurements, the measurements tend to be temporally grouped (i.e., many continuous measurements may be made over a short period of time, but intermittently thereafter) and the error of the mean does not represent an appropriate error range. Instead, the standard deviation of the mean ( $1\sigma$ ) is used for the lidar data to provide an estimate of the strong temporal variability within the layer. There is satisfactory agreement between the OSIRIS and lidar profiles in terms of the peak layer height, full width at half maximum, and absolute densities (within the given error ranges). Differences likely arise as a result of the high variability of the K layer and the spatiotemporal differences between the data observations. In addition to comparing a zonal mean (OSIRIS) with a point measurement (lidar), while OSIRIS makes daylight measurements only, the lidar data sets represent nightly observations (Arecibo) or a diurnal average (Kühlungsborn). The high-altitude secondary

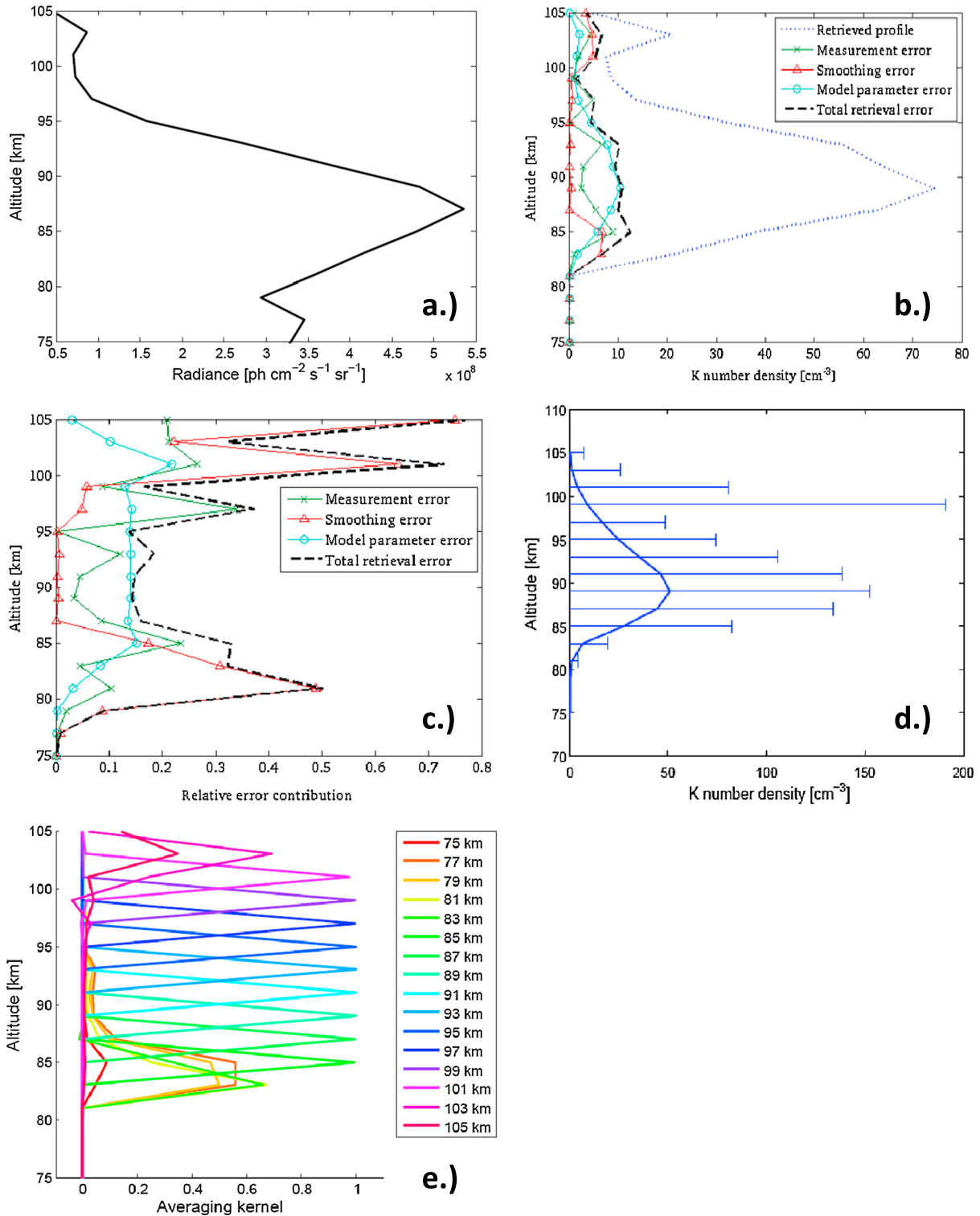


**Figure 2.** (a) Example K integrated radiance profile and (b) resulting retrieved density profile for 3 June 2004,  $-14.55^\circ\text{N}$ ,  $103.61^\circ\text{E}$ , with associated error contributions. (c) The total relative error and error contributions to the example density profile. (d) The a priori K density along with the associated covariance. (e) The averaging kernels for the retrieval.

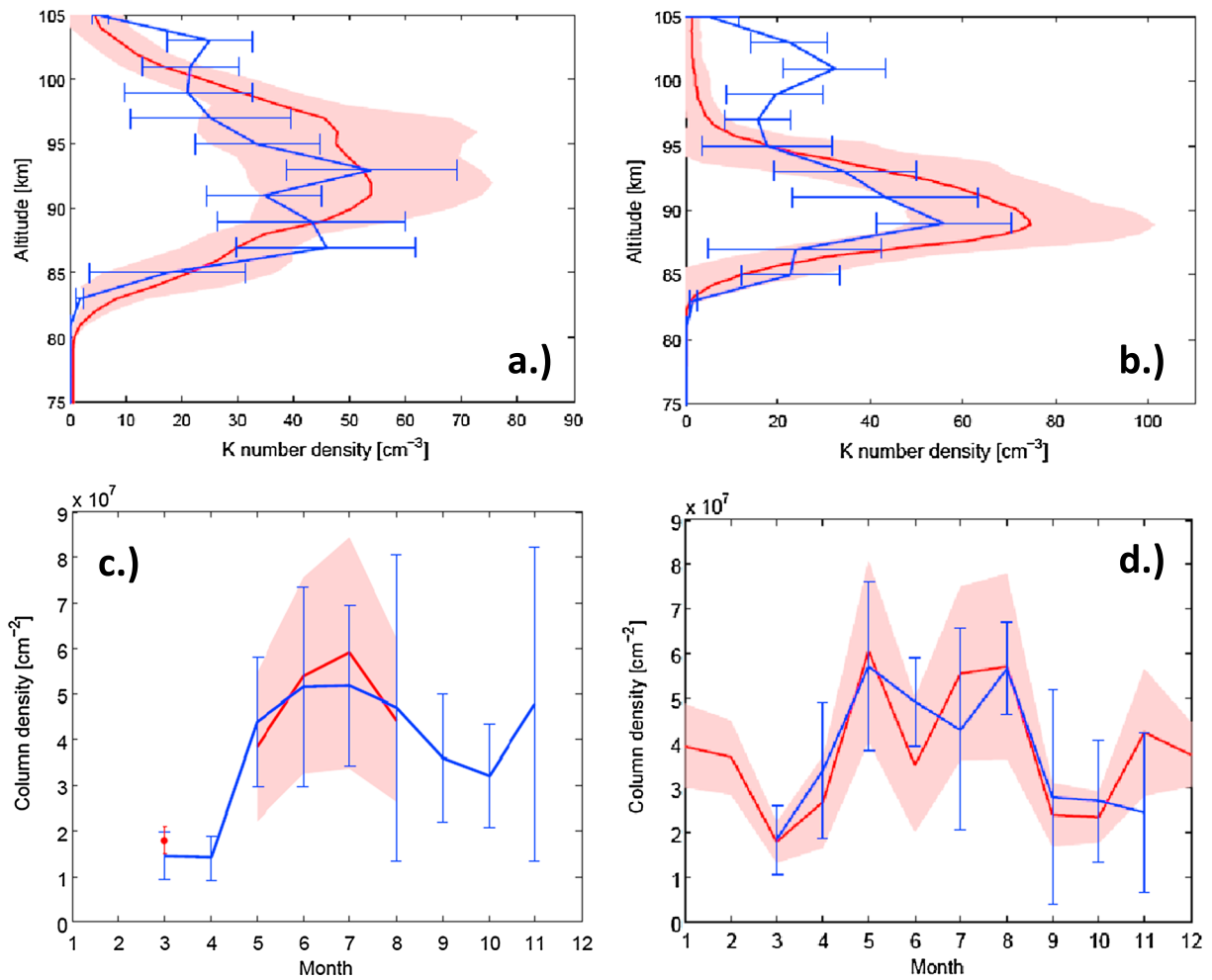


**Figure 3.** (a) OSIRIS versus Arecibo mean monthly K number density profile for July 2004. The monthly mean OSIRIS profile for  $18 \pm 5^\circ\text{N}$  (centered around the Arecibo latitude of  $18^\circ\text{N}$ , consisting of 13 individual profiles) is shown (in blue) along with the corresponding error of the mean ( $2\sigma$ ) (horizontal bars). The corresponding monthly mean lidar profile for Arecibo (consisting of six nightly profiles) is shown (red) along with the associated variability (shaded area,  $1\sigma$ ). See main text for further description. (b) OSIRIS ( $54 \pm 5^\circ\text{N}$ , 11 individual profiles) versus K hlungsborn ( $54^\circ\text{N}$ , seven nights) monthly mean K number density profile for July 2005. Color key same as before and in subsequent panels. (c) OSIRIS versus Arecibo monthly variation of the K column abundance near  $18^\circ\text{N}$  for March–November 2004. (d) OSIRIS versus K hlungsborn monthly K column abundance comparison for 2005. In Figures 3c and 3d, only number densities below  $<97$  km are used in order to minimize the impact of sporadic layers on the analysis. Only satellite and lidar data with more than one day of measurements are used. See text for details of monthly mean profiles.

peak in the OSIRIS ( $54 \pm 5^\circ\text{N}$ ) monthly profile could be a result of the instrument detecting strong topside variability or sporadic K layers not viewed by the lidar instrument. *H ffner and Friedman [2004, 2005]* demonstrate that the summer K layer extends well into the thermosphere ( $>130$  km) and exhibits strong variations, varying by an order of magnitude within timescales of a few hours or more. Seven out of 11 OSIRIS profiles for July 2005 were observed on 1 July, and it is likely that the OSIRIS instrument is observing variability not seen during the lidar observations due to this strong temporal K layer dependence.

The column density represents a more robust measure for comparison. The OSIRIS column densities are compared to the corresponding Arecibo lidar data in Figure 3c for 2004. Only data between 75 and 97 km are used in order to minimize the impact of highly variable sporadic layers, which occur predominantly above this altitude (similar to an approach acknowledged or used in other lidar studies, e.g., *Eska et al. [1998, 1999]*, *Friedman et al. [2002]*, and *Fricke-Begemann et al. [2002]*). The monthly OSIRIS mean column density profiles for March–November 2004 are composed of 21, 6, 15, 23, 13, 5, 16, 13, and 4 individual profiles, respectively. The Arecibo monthly mean column density profiles for March and May–August consist of two, and two, three, six, and seven nightly profiles. There is good agreement during the period March–June 2004, with both the OSIRIS and lidar data capturing the pronounced summer

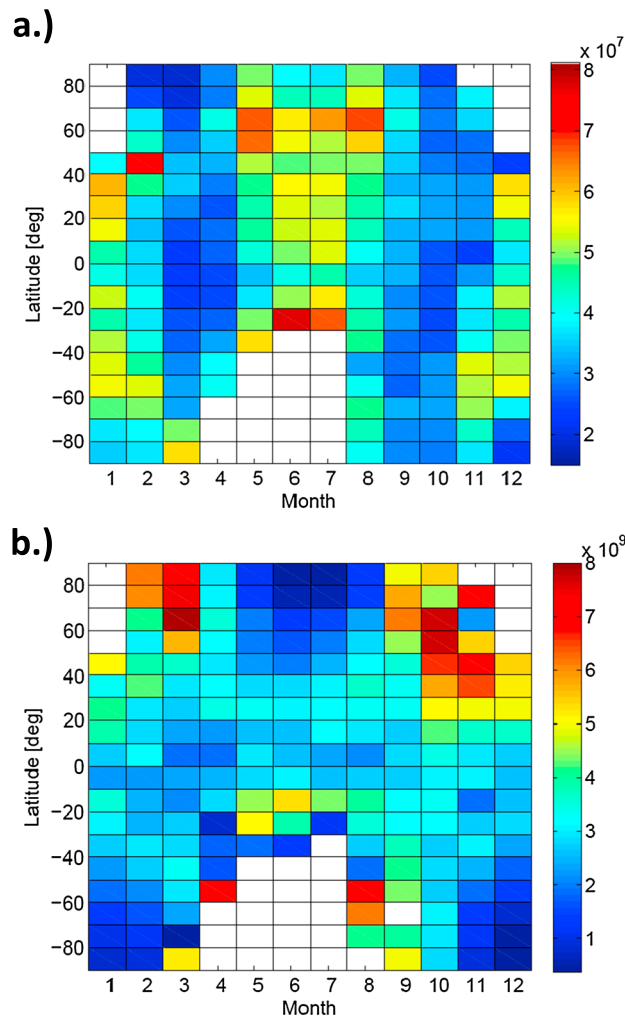


**Figure 4.** (a) Grid plot of the monthly averaged total K column density ( $10^7 \text{ cm}^{-2}$ ) zonally averaged in  $10^\circ$  latitude bins for 2004–2011. (b) Equivalent plot for the monthly averaged total Na column density ( $10^9 \text{ cm}^{-2}$ ) (also retrieved from OSIRIS) for 2004–2011. Only metal number densities below  $<97 \text{ km}$  are used in order to minimize the impact of sporadic layers on the analysis.

at very high latitudes. The summertime depletion of the layer at high latitudes ( $>70^\circ$ ) is likely as a result of removal of metal atoms by polar mesospheric clouds, supporting the work of *Raizada et al.* [2007]. Figure 4b is the analogous plot for the Na layer column abundance, also retrieved from OSIRIS observations [*Fan et al.*, 2007]. Note the deep summertime minimum seen in the Na layer at high latitudes, where the summer:winter ratio approaches 1:10 and the absence of seasonal variation at low latitudes. In contrast, the semiannual seasonal behavior of the K layer shows little latitudinal variation.

### 6. Conclusions

We have described the first measurement of the near-global K layer from space-borne observations of resonance fluorescence in the dayglow. The retrieval technique is capable of determining profiles with a total uncertainty of  $\pm 15\%$  at the peak of the layer, and an altitude resolution of 2 km. While the forward model takes into account the spectral background shape, local albedo, and self-absorption, it neglects the Ring effect, which was found to have a negligible effect on the final retrieved density profile. Within the peak region, the largest source of error is the model parameter error, specifically errors associated with

maximum. Any differences between the data are likely due to there being limited periods within each month where both OSIRIS and the lidar are operating concurrently. In these months, there were only a very limited numbers of measurements made at Arecibo; it is possible that some individual events (such as enhanced K densities during sporadic layer activity, particularly those occurring above 97 km) seen in the satellite instrument may not have been seen by the lidar during the same period.

Figure 3d shows the equivalent monthly column density comparison between OSIRIS and Kühlungsborn data for 2005. The zonal monthly OSIRIS mean column density profiles for March–November 2005 consist of 20, 13, 3, 37, 11, 20, 4, 10, and 3 profiles, respectively. The Kühlungsborn mean monthly column densities are composed of 7, 5, 9, 14, 3, 16, 7, 7, 9, 16, 3, and 3 individual nightly mean profiles. There is largely very good agreement between the months of April and November with a summertime maximum and equinoctial minima being observed in both. A midsummer local minimum exists in both data sets, but the OSIRIS minimum occurs one month later than in the lidar data.

### 5. The Near-Global Retrieved K Layer

Figure 4a illustrates the first near-global observations of the K layer. This demonstrates that the semiannual variability seen previously at extratropical locations is, in fact, global in extent, except

determining the albedo contribution to the instrument line of sight, and also to the calculation of the solar irradiance reference flux.

Monthly absolute number density profiles and column densities are satisfactorily ground-truthed with available lidar data from the Arecibo and Kühlungsborn stations (for 2004 and 2005, respectively). The unusual semiannual behavior of the K layer is shown to occur at all latitudes with satellite coverage.

In a future publication we will exploit this new near-global data set, in particular using it to inform atmospheric modeling studies of K metal chemistry and related processes.

#### Acknowledgments

This work was funded by the UK Natural Environment Research Council (grant NE/G019487/1). The Arecibo Observatory is operated by a consortium led by SRI International and including the Universidad Metropolitana and Universities Space Research Association under a cooperative agreement with the U.S. National Science Foundation. The K lidar data at Arecibo are available at <http://www.naic.edu/aisr/database/data/lidar/> archive, the Kühlungsborn lidar potassium data are available upon request to J.H., and the satellite retrieved data are available upon request to J.M.C.P.

The Editor thanks two anonymous reviewers for their assistance in evaluating this paper.

#### References

- Akmaev, R. A. (2011), Whole atmosphere modeling: Connecting terrestrial and space, *Rev. Geophys.*, *49*, RG4004, doi:10.1029/2011RG000364.
- Akmaev, R. A., V. I. Fomichev, and X. Zhu (2006), Impact of middle-atmospheric composition changes on greenhouse cooling in the upper atmosphere, *J. Atmos. Sol. Terr. Phys.*, *68*, 1879–1889, doi:10.1016/j.jastp.2006.03.008.
- Chance, K. V., and R. J. Spurr (1997), Ring effect studies: Rayleigh scattering, including molecular parameters for rotational Raman scattering, and the Fraunhofer spectrum, *Appl. Opt.*, *36*, 5224–5230, doi:10.1364/AO.36.005224.
- Chandran, A., R. L. Collins, R. R. Garcia, D. R. Marsh, V. L. Harvey, J. Yue, and L. de la Torre (2013), A climatology of elevated stratopause events in the whole atmosphere community climate model, *J. Geophys. Res. Atmos.*, *118*, 1234–1246, doi:10.1002/jgrd.50123.
- Dee, D. P., et al. (2011), The ERA-Interim reanalysis: Configuration and performance of the data assimilation system, *Q. J. R. Meteorol. Soc.*, *137*(656), 553–597, doi:10.1002/qj.828.
- Delgado, R., J. S. Friedman, J. T. Fentzke, S. Raizada, C. A. Tepley, and Q. Zhou (2012), Sporadic metal atom and ion layers and their connection to chemistry and thermal structure in the mesopause region at Arecibo, *J. Atmos. Sol. Terr. Phys.*, *74*, 11–23, doi:10.1016/j.jastp.2011.09.004.
- Eska, V., J. Höffner, and U. von Zahn (1998), Upper atmosphere potassium layer and its seasonal variations at 54°N, *J. Geophys. Res.*, *103*, 29,207–29,214, doi:10.1029/98JA02481.
- Eska, V., U. von Zahn, and J. M. C. Plane (1999), The terrestrial potassium layer (75–110 km) between 71°S and 54°N: Observations and modeling, *J. Geophys. Res.*, *104*, 17,173–17,186, doi:10.1029/1999JA900117.
- Fan, Z. Y., J. M. C. Plane, J. Gumbel, J. Stegman, and E. J. Llewellyn (2007), Satellite measurements of the global mesospheric sodium layer, *Atmos. Chem. Phys.*, *7*, 4107–4115, doi:10.5194/acp-7-4107-2007.
- Feng, W., D. R. Marsh, M. P. Chipperfield, D. Janches, J. Höffner, F. Yi, and J. M. C. Plane (2013), A global atmospheric model of meteoric iron, *J. Geophys. Res. Atmos.*, *118*, 9456–9474, doi:10.1002/jgrd.50708.
- Fricke-Begemann, C., J. Höffner, and U. von Zahn (2002), The potassium density and temperature structure in the mesopause region (80–105 km) at a low latitude (28°N), *Geophys. Res. Lett.*, *29*(22), 2067, doi:10.1029/2002GL015578.
- Friedman, J. S., S. C. Collins, R. Delgado, and P. A. Castleberg (2002), Mesospheric potassium layer over the Arecibo Observatory, 18.3N 66.75W, *Geophys. Res. Lett.*, *29*, 15-1–15-4, doi:10.1029/2001GL013542.
- Fussen, D., et al. (2004), Global measurement of the mesospheric sodium layer by the star occultation instrument GOMOS, *Geophys. Res. Lett.*, *31*, L24110, doi:10.1029/2004GL021618.
- Fussen, D., et al. (2010), A global climatology of the mesospheric sodium layer from GOMOS data during the 2002–2008 period, *Atmos. Chem. Phys.*, *10*, 9225–9236, doi:10.5194/acp-10-9225-2010.
- Gardner, J. A., R. A. Viereck, E. Murad, D. J. Knecht, C. P. Pike, A. L. Broadfoot, and E. R. Anderson (1995), Simultaneous observations of neutral and ionic magnesium in the thermosphere, *Geophys. Res. Lett.*, *22*, 2119–2122, doi:10.1029/95GL01769.
- Gumbel, J., Z. Y. Fan, T. Waldemarsson, J. Stegman, G. Witt, E. J. Llewellyn, C.-Y. She, and J. M. C. Plane (2007), Retrieval of global mesospheric sodium densities from the Odin satellite, *Geophys. Res. Lett.*, *34*, L04813, doi:10.1029/2006GL028687.
- Hedin, A. E. (1991), Extension of the MSIS thermosphere model into the middle and lower atmosphere, *J. Geophys. Res.*, *96*, 1159–1172, doi:10.1029/90JA02125.
- Hedin, J., and J. Gumbel (2011), The global mesospheric sodium layer observed by Odin/OSIRIS in 2004–2009, *J. Atmos. Sol. Terr. Phys.*, *73*, 2221–2227, doi:10.1016/j.jastp.2010.10.008.
- Höffner, J., and J. S. Friedman (2004), The mesospheric metal layer topside: A possible connection to meteoroids, *Atmos. Chem. Phys.*, *4*, 801–808, doi:10.5194/acp-4-801-2004.
- Höffner, J., and J. S. Friedman (2005), The mesospheric metal layer topside: Examples of simultaneous metal observations, *J. Atmos. Solar-Terr. Phys.*, *67*, 1226–1237, doi:10.1016/j.jastp.2005.06.010.
- Höffner, J., and F.-J. Lübken (2007), Potassium lidar temperatures and densities in the mesopause region at Spitsbergen (78°N), *J. Geophys. Res.*, *112*, D20114, doi:10.1029/2007JD008612.
- Höffner, J., C. Fricke-Begemann, and F.-J. Lübken (2003), First observations of noctilucent clouds by lidar at Svalbard, 78°N, *Atmos. Chem. Phys.*, *3*, 1101–1111, doi:10.5194/acp-3-1101-2003.
- Hurrell, J. W., et al. (2013), The Community Earth System Model: A framework for collaborative research, *Bull. Am. Meteorol. Soc.*, *94*(9), 1339–1360, doi:10.1175/BAMS-D-12-00121.1.
- Kramida, A., Y. Ralchenko, J. Reader, and NIST ASD Team (2013), NIST Atomic Spectra Database (ver. 5.1). [Available at <http://physics.nist.gov/asd/>].
- Langowski, M., M. Sinnhuber, A. C. Aikin, C. von Savigny, and J. P. Burrows (2014a), Retrieval algorithm for densities of mesospheric and lower thermospheric metal atom and ion species from satellite-borne limb emission signals, *Atmos. Meas. Tech.*, *7*, 29–48, doi:10.5194/amt-7-29-2014.
- Langowski, M., C. von Savigny, J. P. Burrows, W. Feng, J. M. C. Plane, D. R. Marsh, D. Janches, M. Sinnhuber, and A. C. Aikin (2014b), Global investigation of the Mg atom and ion layers using SCIAMACHY/Envisat observations between 70 km and 150 km altitude and WACCM-Mg model results, *Atmos. Chem. Phys. Discuss.*, *14*, 1971–2019, doi:10.5194/acpd-14-1971-2014.
- Laštovička, J. (2006), Global change in the upper atmosphere, *Science*, *314*(5803), 1253–1254, doi:10.1126/science.1135134.
- Lide, D. R. (2006), *Handbook of Physics and Chemistry*, 87th ed., CRC Press, Boca Raton, Fla.
- Llewellyn, E. J., et al. (2004), The OSIRIS instrument on the Odin spacecraft, *Can. J. Phys.*, *422*, 411–422, doi:10.1139/P04-005.
- Lübken, F.-J., and J. Höffner (2004), Experimental evidence for ice particle interaction with metal atoms at the high latitude summer mesopause region, *Geophys. Res. Lett.*, *31*, L08103, doi:10.1029/2004GL019586.

- Marsh, D. R., D. Janches, W. Feng, and J. M. C. Plane (2013), A global model of meteoric sodium, *J. Geophys. Res. Atmos.*, *118*, 11,442–11,452, doi:10.1002/jgrd.50870.
- Mégie, G., F. Bos, and M. L. Chanin (1978), Simultaneous nighttime lidar measurements of atmospheric sodium and potassium, *Planet. Space Sci.*, *26*, 27–35, doi:10.1016/0032-0633(78)90034-X.
- Murtagh, D., et al. (2002), An overview of the Odin atmospheric mission, *Can. J. Phys.*, *319*, 309–319, doi:10.1139/P01-157.
- Plane, J. M. C. (2003), Atmospheric chemistry of meteoric metals, *Chem. Rev.*, *103*, 4963–4984, doi:10.1021/cr0205309.
- Plane, J. M. C. (2012), Cosmic dust in the Earth's atmosphere, *Chem. Soc. Rev.*, *41*, 6507–6518, doi:10.1039/c2cs35132c.
- Raizada, S., M. Rapp, F.-J. Lübken, J. Höffner, M. Zecha, and J. M. C. Plane (2007), Effect of ice particles on the mesospheric potassium layer at Spitsbergen (78°N), *J. Geophys. Res.*, *112*, D08307, doi:10.1029/2005JD006938.
- Roble, R. G., and R. E. Dickinson (1989), How will changes in carbon dioxide and methane modify the mean structure of the mesosphere and thermosphere?, *Geophys. Res. Lett.*, *46*, 1441–1444, doi:10.1029/GL016i012p01441.
- Rodgers, C. D. (2000), *Inverse Methods for Atmospheric Sounding: Theory and Practice*, World Scientific Publishing Co., Singapore.
- Scharringhausen, M., A. C. Aikin, J. P. Burrows, and M. Sinnhuber (2008a), Space-borne measurements of mesospheric magnesium species—A retrieval algorithm and preliminary profiles, *Atmos. Chem. Phys.*, *8*, 1963–1983, doi:10.5194/acp-8-1963-2008.
- Scharringhausen, M., A. C. Aikin, J. P. Burrows, and M. Sinnhuber (2008b), Global column density retrievals of mesospheric and thermospheric Mg I and Mg II from SCIAMACHY limb and nadir radiance data, *J. Geophys. Res.*, *113*, D13303, doi:10.1029/2007JD009043.
- Von Zahn, U., and J. Höffner (1996), Mesopause temperature profiling by potassium lidar, *Geophys. Res. Lett.*, *23*, 141–144, doi:10.1029/95GL03688.